Advances and Applications in Fluid Mechanics
Volume 11, Number 2, 2012, Pages 87-117
Available online at http://pphmj.com/journals/aafm.htm
Published by Pushpa Publishing House, Allahabad, INDIA

NUMERICAL AND EXPERIMENTAL EXPLORATION OF FLOW THROUGH A TEETH-SHAPED NOZZLE

A. Van Hirtum[1], X. Grandchamp[1], J. Cisonni[2], K. Nozaki[3] and H. Bailliet[4]

[1]GIPSA-lab, UMR CNRS 5216
Grenoble University
France

[2]Center for Advanced Medical Engineering and Informatics
Osaka University
Japan

[3]Graduate School of Engineering Science
Osaka University
Japan

[4]Institut P′ CNRS
Université de Poitiers, ENSMA
Département Fluides Thermique Combustion, ENSIP
6 rue Marcel Doré, Bâtiment B17-BP633
86022 Poitiers Cedex, France

Abstract

An asymmetrical constricted rectangular nozzle is designed representing upper incisors in the oral tract. Steady flow through the nozzle is studied for a fixed constriction degree of 70% and bulk

2010 Mathematics Subject Classification: 76Zxx, 76Mxx, 76Gxx.

Keywords and phrases: subsonic jet, human upper airway, biological flow, LES, PIV, smoke visualisation.

Received January 30, 2012

Reynolds number $\mathrm{Re}_b = 4000$. Flow data are obtained numerically by Large Eddy Simulation as well as experimentally from smoke visualisation and from Particle Image Velocimetry. Quantitative and qualitative exploration of the mean and fluctuating properties of the flow field reveals the impact of the obstacle's presence on the overall flow field and stresses the need for future in depth studies of the impact of geometrical parameters.

1. Introduction

Aerodynamic and aeroacoustic principles have been introduced in speech production studies dealing with sibilant fricatives since Fant [8]. Since then, the underlying mechanism of sibilant fricative sound production is generally described as noise produced due to the interaction of a turbulent jet, issued from a constriction somewhere in the vocal tract, with a downstream wall or obstacle [34, 15, 28]. Fant's pioneering work [8] has been further developed in experimental as well as modeling studies (e.g., [34, 36, 1, 27, 15, 17, 35, 40]). Nevertheless, most of the previous studies focus on the acoustics of fricative noise production and not on the flow. In fact, there are few studies that provide flow data for configurations relevant to human sibilant fricative production, i.e., moderate bulk Reynolds numbers $\mathrm{Re}_b = U_b h/\nu$ covering the range $\mathrm{Re}_b < 10^4$ [38] and low Mach number $M < 0.3$ with mean bulk velocity U_b, characteristic height h, kinematic viscosity ν, speed of sound c and $M = U_b/c$. Therefore, additional flow data are necessary in order to increase understanding about the fundamental processes of sibilant fricative sound generation [15, 3].

A major difficulty of the flow configuration under study lies in the fact that the Reynolds number range $\mathrm{Re}_b < 10^4$ includes the transition Reynolds number of diffuser flow as well as the critical Reynolds number of pipe flows so that the flow regime is complex and highly dependent on initial conditions triggering transition [32]. In addition, due to the presence of different vocal tract articulators - such as tongue, glottis and tooth - the variation in real life geometry is extremely complex causing initial flow conditions to vary as

well. In order to facilitate reliable interpretation of flow data, the real life geometry and flow conditions in the current study are extremely simplified following the approach presented in [34, 12, 40]. The current study focuses on flow through a nozzle containing an obstacle of fixed shape, which represents an upper incisor. The flow is studied for laminar inlet flow at a single Reynolds number $\mathrm{Re}_b = 4000$.

An upper incisor is represented by a trapezoid wedge [12]. The obstacle is inserted in a rectangular channel perpendicular to the main flow direction which results in a simple 'in-vitro' replica representing the vocal tract containing a single upper incisor. Consequently, flow development through a simplified tooth-shaped nozzle can be studied. The constriction degree is fixed to 70%. The width-to-height aspect ratio is 4 in the unconstricted channel and 15 within the constriction so that the flow is considered as two-dimensional which facilitates experimental flow characterisation. Despite the simplifications, a complex near field flow pattern is expected to occur downstream from the obstacle due to the interaction between two generic layers, i.e., an inner layer adjacent to the flat wall and an outer layer due to flow separation downstream from the obstacle tip. Preliminary measurements using single sensor anemometry in the near field downstream from the tooth edge up to the channel exit confirmed the existence of two generic layers as well as the two-dimensional nature of the flow at the obstacle tip [12]. Nevertheless, a spatial overall view of the flow development is not assessed whereas such an overall view is needed in order to improve characterisation of the flow field and to identify the relevance of the geometrical parameters used to design the proposed simplified tooth-shaped nozzle for future in depth studies.

Consequently, the current exploratory study aims to contribute to the overall characterisation and understanding of the flow field issuing from a tooth-shaped nozzle, the resulting combination of shear and jet flow and the development of simplified geometries suitable to study flow through the vocal tract. A computational grid and matching experimental nozzle are used to provide quantitative and qualitative data of the mean and fluctuating flow

development. The flow field is studied numerically by Large Eddy Simulation (LES) as well as experimentally by smoke visualisation and Particle Image Velocimetry (PIV). Although a more in depth characterisation is necessary, it is shown that both quantitative and qualitative approaches allow to capture main features of the velocity field. As such, all assessed approaches are suitable to obtain an overall view of the velocity field for the nozzle under study. Compared to LES and PIV, smoke visualisation has the advantage to provide qualitative information in a straightforward and non-expensive way for which the data can be processed without any computational cost. Consequently, smoke visualisation is suitable to select configurations of interest prior to a quantitative study combining numerical simulation and PIV experiments in order to obtain accurate data which can be validated.

2. Tooth-shaped Nozzle Geometry

The geometry of the tooth-shaped nozzle [12] is based on two main morphological characteristics [30, 6, 9, 24, 23]: (1) upper incisor dimensions in the flow direction and (2) upper incisor position with respect to the palatal plane. The nozzle is schematically depicted in Figure 1 and the main geometrical parameters are summarised in Table 1.

The nozzle consists of a tooth-shaped obstacle inserted in a rectangular channel. The uniform channel has width $w = 105\text{mm}$, unconstricted channel height $h_0 = 25\text{mm}$ and total length l_{noz}. The tooth-shaped obstacle consists of a trapezoid defined by its base $l_{pal} = 6.6\text{mm}$ [6, 9], tip length $l_t = 1.25\text{mm}$ [29] and height $h_t = 17.5\text{mm}$ [23]. The base of the trapezoid is a portion of the palatal plane represented by the upper plane of the rectangular channel. Consequently, when inserting the obstacle in the unconstricted channel, the leading and trailing angles of the tooth-shaped obstacle with the upper plane of the rectangular channel are $\theta_1 = 107^\circ$ and $\theta_2 = 90^\circ$ which correspond to the order of magnitudes reported for *in-vivo* measurements on living subjects [6, 9]. Next, the tooth-shaped obstacle is inserted $l_0 = 11\text{mm}$ upstream of the nozzle outlet in order to respect the morphological distance

between the trailing tooth edge and the trailing lip position approximated as $l_0 \approx 1.7 \times l_{pal}$ [24]. The resulting minimum aperture at the obstacle yields $h = 7.5\text{mm}$. The contraction ratio h_0/h yields about 3 resulting in a ±70% obstruction degree at the tooth obstacle. The ratios of (1) the obstacle length l_{pal} and (2) the channel downstream the constriction l_0 to the minimum aperture yield $l_{pal}/h = 0.88$ and $l_0/h = 1.5$. Finally, note that the aspect ratios of the tooth-shaped nozzle, both in the unconstricted and constricted regions, are superior to 1, $w/h_0 \approx 4$ and $w/h \approx 15$. Consequently, the flow is expected to be statistically similar to a two-dimensional flow [26].

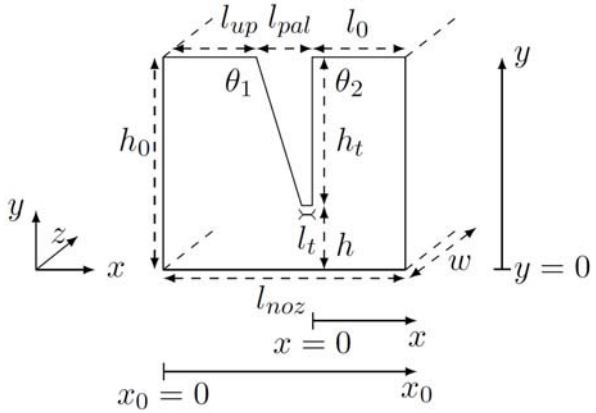

Figure 1. Schematic representation of the tooth-shaped nozzle: unconstricted channel height $h_0 = 25\text{mm}$, uniform channel width $w = 105\text{mm}$, minimum aperture height $h = 7.5\text{mm}$, obstacle height $h_t = 17.5\text{mm}$, obstacle tip length $l_t = 1.25\text{mm}$, obstacle base length $l_{pal} = 6.6\text{mm}$, length from the obstacle trailing edge up to the nozzle outlet $l_0 = 11\text{mm}$, length from the nozzle inlet to the obstacle leading edge l_{up}, total nozzle length $l_{noz} = l_{up} + l_{pal} + l_0$, $\theta_1 = 107^\circ$ and $\theta_2 = 90^\circ$ the obstacles leading and trailing edge angles. The *x*-axis in the streamwise direction corresponds to the main flow direction, the *y*-axis to the transverse direction and the *z*-axis is taken along the spanwise direction. In addition, the inlet of the nozzle is denoted $x_0 = 0$ and the trailing edge of the obstacle corresponds to $x = 0$.

Table 1. Main geometrical parameters of the proposed tooth-shaped nozzle

Parameter	Symbol	Value
Channel downstream length	l_0	11mm
Constriction aperture	h	7.5mm
Constriction length	l_t	1.25mm
Channel height	h_0	25mm
Channel width	w	105mm
Obstacle upstream angle	θ_1	107°
Obstacle downstream angle	θ_2	90°
Channel upstream length	l_{up}	92.4mm
Total channel length	l_{noz}	110mm

3. Numerical Simulation

The airflow is simulated with Large Eddy Simulation (LES) for incompressible unsteady flows [20, 31]. The subgrid scale turbulence is modelled with the dynamic Smagorinsky model. The physical model and governing equations are outlined in Appendix A. The equations are implemented in a general-purpose finite element code *Front Flow Blue*/*FFB5* [16, 13]. Simulations are performed using a vector supercomputer (SX8 NEC Inc.). The spatially-filtered momentum equation (1) and continuity equation (2) are solved over the discretised flow domain matching the geometry of the tooth-shaped nozzle described in Section 2 and summarised in Table 1. The inlet length of the channel upstream from the obstacle is set to $l_{up} = 92.4\text{mm}$. Therefore, the total length of the computational channel yields $l_{noz} = 110\text{mm}$.

Spatial discretisation is carried out using Gridgen (Pointwise Inc.). A structured mesh is defined using hexahedral finite elements. The accuracy of the mesh in the transverse direction is increased near the walls to resolve the boundary layer. Furthermore, the mesh sizes in the streamwise Δ_x and

transverse Δ_y direction are finer in the constricted region and in the region downstream the constriction where the jet is located to resolve rapid variation of the flow properties and bound vortices around the obstacle. The flow is assumed to be statistically two-dimensional so that only slow variation of the flow properties in the spanwise z direction is expected. Therefore, the element size in the spanwise z direction is less accurate than in the streamwise x and transverse y direction, i.e., $\Delta_z > \Delta_x$ and $\Delta_z > \Delta_y$. Finally, the sizes of the elements are chosen to ensure stability of the flow model. The quality of the mesh is verified with respect to minimum vertex angle, maximum face skewness, minimum element size and node distribution. Mesh features are summarised in Table 2. The characteristic length scale of the boundary layer $l = \nu/u^*$ is estimated from the ratio of the kinematic viscosity ν and the friction velocity $u^* = \sqrt{\tau_p/\rho_0}$ using the relationship $\tau_p = 0.079\,\mathrm{Re}_b^{-1/4}$ and the values for Re_b, ν and density ρ_0 indicated in Table 3 [32]. It is noted that the resulting characteristic length scale of the boundary layer yields $l = 0.2\mathrm{mm}$ so that $\Delta_y < l$ holds so that the applied averaged transverse Δ_y near the boundaries is sufficiently small to resolve the boundary layer.

Table 2. Main discretisation parameters

Total number of elements	1882200
Averaged Δ_x at the constriction	0.089mm
Averaged Δ_y at the constriction	0.12mm
Averaged Δ_y at the boundaries	0.050mm
Averaged Δ_z	2.6mm

A uniform velocity profile is imposed at the inlet of the computational domain. No-slip boundary conditions are used at the wall whereas non-reflective conditions are imposed at the outlet. To ensure numerical stability of the model, the non-dimensional time increment is set so that $10^{-3} =$

$\Delta t \cdot U_b/h_0$ with U_b the bulk velocity at the inlet and h_0 the unconstricted nozzle height in accordance with Figure 1. The Reynolds number yields $\mathrm{Re}_b = 4000$, so that the bulk velocity at the inlet yields $U_b = 2.4\,\mathrm{m/s}$ and the volume airflow rate yields $\phi = 363\,\mathrm{l/min}$. Mean and fluctuating flow characteristics are quantified on instantaneous flow fields spanning 52ms. Simulation parameters are summarised in Table 3. The chosen time step Δt satisfies the Courant-Friedrichs-Lewy condition (CFL). The CFL-number remains constant after 3000 time steps and its value yields 0.6. The contribution of the subgrid scale model to the energy spectrum is 9%.

Table 3. Simulation parameters and monitored values

Parameter	Value
Inlet velocity U_b	$2.4\mathrm{m.s}^{-1}$
Bulk Reynolds number Re_b	4000
Volume airflow rate ϕ	363l/min
Air density ρ_0	$1.2\mathrm{kg.m}^{-3}$
Air kinematic viscosity ν	$1.5\times10^{-5}\mathrm{m}^2\mathrm{.s}^{-1}$
Time step Δt	$1\times10^{-5}\mathrm{s}$
Total simulation time T_{sim}	130ms
Time used to calculate flow statistics T_m	52ms
Total number of time steps N_{tot}	13000
Number of time steps used for flow statistics N_m	5200
Courant-Friedrichs-Lewy condition *CFL*	0.6
Smagorinsky constant C_S	< 0.002
Subgrid scale contribution	9%

4. Experimental Setup and Smoke Experiment

The experimental approach is based on an in-vitro mechanical replica of the tooth-shaped nozzle described in Section 2. A rigid *in-vitro* replica,

matching the nozzle depicted in Figure 1, is obtained by inserting a plain trapezoid wedge in a transparent rectangular channel. The transparent walls of the *in-vitro* replica have thickness 5.5mm. The nozzle is mounted in an experimental setup enabling one to perform qualitative and quantitative flow visualisation experiments using smoke injection by means of a fog machine. Airflow is generated in a flow facility consisting of an air compressor (Atlas Copco GA7). Downstream, a pressure regulator (Norgren type 11-818-987) and a manual valve enable one to provide a constant air pressure. The manual valve is connected to a mass flow meter (TSI 4040) via a uniform duct of diameter 0.01m. Next, the uniform duct connects the mass flow meter to a settling chamber of volume 0.112m^3 (with dimensions $56 \times 50 \times 40\text{cm}$ $\text{length} \times \text{height} \times \text{width}$) to which the rigid 'in-vitro' nozzle is attached. Grids are placed in the settling chamber in order to reduce the turbulence intensity. A schematic overview of the flow visualisation setup is given in Figure 2.

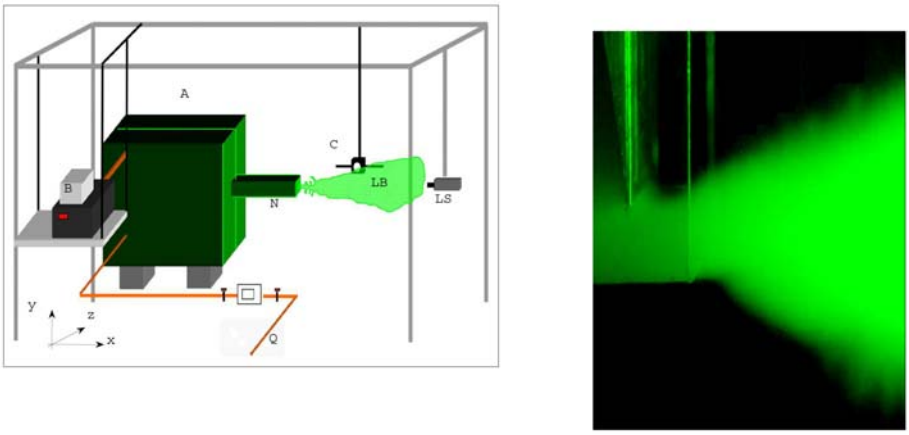

(a) (b)

Figure 2. (a) Schematic representation of the experimental setup for smoke experiments: (1) flow settling chamber (A) of volume 0.112m^3 with dimensions $56 \times 50 \times 40\text{cm}$ to which the nozzle (N) represented in Figure 1 is attached, (2) smoke generation and injection (B), (3) volume airflow rate supply (Q) with pressure regulator and thermal mass flow meter, (4) laser source (LS), (5) camera (C) perpendicular to the laser sheet (LB). The laser

source (LS) and camera (C) are mounted on a three-dimensional rail system. The axes are as defined in Figure 1, so that the x-axis indicates the main flow direction and the origin is again as defined in Figure 1. (b) Example of two-dimensional $(x,\ y)$ instantaneous flow visualisation image.

To allow comparison between the experimental and computational flow field, the volume airflow rate Q is fixed to $Q = 3631/\text{min}$ corresponding to bulk Reynolds number $\text{Re}_b = 4000$ in agreement with values given in Table 3. The streamwise turbulence intensity at the nozzle inlet, measured by constant temperature anemometry (IFA300 and single sensor hot film TSI 1201-20) is less than 1% [12]. Smoke experiments are performed downstream from the obstacle and downstream from the nozzle exit. These smoke experiments enable to validate the simulated flow field downstream from the obstacle up to the nozzle exit. In addition, the performed smoke experiments provide an overall view of the flow field downstream from the nozzles exit which is lacking in the numerical data.

Both qualitative and quantitative smoke experiments are performed by considering the image flow field and the velocity flow field, respectively. The image flow field is studied by processing individual images, such as shown in Figure 2(b), in order to estimate the instantaneous spatial distribution of smoke concentration from the scattered light intensity following standard methods [14, 25, 37]. Since the studied flow is two-dimensional [12], as are the images, the image-flow velocity field is assumed to be a good representation of the fluid-flow velocity field [39, 22]. Therefore, calculation of the image flow field statistics provides qualitative information of the velocity field. The followed approach is detailed in Appendix B.1. The used visualised window is approximately $17\text{cm} \times 17\text{cm}$ and covers the region downstream from the obstacle tip up to $0 < x/h < 7$. Consequently, the simulated flow field can be compared qualitatively with the image flow field in the region downstream from the obstacle up to the nozzles exit, i.e., $0 < x/h < 1.5$. In addition, an overall view of the flow development downstream from the nozzle exit is obtained, i.e., $1.5 < x/h < 7$.

Quantitative information of the velocity field is obtained by Particle Image Velocimetry (PIV) measurements. The applied PIV measurement consists in capturing two successive images of the particles present in the flow. Measuring the displacement of the particles and knowing the time separation *Dt* between the two images allows to deduce the velocity using correlation procedures [2]. The applied PIV procedure is detailed in Appendix B.2. Two measurement zones are assessed. A measurement zone of approximately $5\text{cm} \times 4\text{cm}$ is used to focus on the velocity flow field in the vicinity of the obstacle, i.e., $-2.1 < x/h < 3.2$. In addition, a measurement zone of $20\text{cm} \times 16\text{cm}$ is used in order to provide an overall view of the velocity flow field of the jet issuing from the nozzle, i.e., $1.5 < x/h < 22$. Flow statistics are quantified on 2000 pair of images.

A summary of the main settings of the performed smoke experiments is given in Table 4.

Table 4. Summary of smoke experiments parameters. The spatial resolution [mm] of the PIV measurements is indicated between brackets $(\Delta x_{PIV}, \Delta y_{PIV})$

Smoke experiment	Visualised window	Window position	Flow field $(\Delta x_{PIV}, \Delta y_{PIV})$ [mm]
Smoke visualisation	$17\text{cm} \times 15\text{cm}$	$0 < x/h < 7$	Image
PIV	$5\text{cm} \times 4\text{cm}$	$-2.1 < x/h < 3.2$	Velocity (0.3, 0.3)
	$20\text{cm} \times 16\text{cm}$	$1.5 < x/h < 22$	Velocity (1.1, 1.2)

5. Results

In the following, the simulated and experimentally assessed flow fields are outlined and their main features are discussed. At first, airflow through the nozzle is discussed based on numerical data. Next, the experimentally assessed qualitative and quantitative flow fields are presented and compared to the simulated flow fields in the region spanning from the obstacle's

trailing edge to the nozzles exit, i.e., $0 < x/h < 1.5$. An overview of the principal characterised quantities is given in Table 5.

Table 5. Overview of principal characterised quantities from Large Eddy Simulation (LES), Particle Image Velocimetry (PIV) and Smoke Visualisation (SV). Root mean square is abbreviated rms

Data	Quantities		
LES	mean velocity U	rms velocity σ	vorticity ω
PIV	mean velocity U^{piv}	rms velocity U_{rms}^{piv}	vorticity ω^{piv}
SV	mean smoke concentration $\bar{I}$	rms smoke concentration I_{rms}	

5.1. Flow through the nozzle: simulated flow field

The streamwise x and transverse y components of the simulated mean velocity field at the center of the nozzle, corresponding to the plane $z = w/2$, are illustrated in Figure 3. The x component is seen to accelerate in the main streamwise direction from 2.4m/s, corresponding to the velocity imposed at the inlet, to a maximum of 13m/s downstream the constriction, which is about 5 times the inlet velocity. Negative velocities occur downstream the obstacle's trailing edge indicating the presence of a recirculation zone. In addition, flow is detached of the obstacles tip at its leading edge, so that flow separation and jet formation occur along the obstacles tip. The y component of the mean velocity yields 0m/s, which is the value imposed at the inlet, except just upstream the obstacle's leading edge where negative values up to –8m/s are reached due to flow acceleration towards the constriction. The spanwise z component of the mean velocity field is omitted in Figure 3 since its mean value over the whole spatial domain is in the range $[-0.5 \;\; 0.5]\,\mathrm{m/s}$ which confirms the two-dimensionality of the flow field.

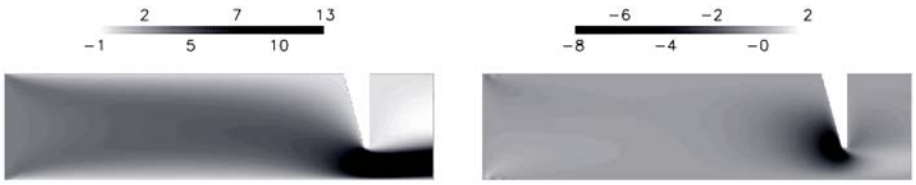

(a) *x*-component U_1 (b) *y*-component U_2

Figure 3. Simulated mean velocity components [m/s] for the plane $(x_0,\ y,\ z = w/2)$.

Transverse profiles of the simulated mean velocity throughout the nozzle $U(x_0,\ y,\ z = w/2)$ are shown in Figure 4. The profile at $x_0 = 0$ corresponds to the imposed uniform velocity profile at the nozzle inlet, $U(x_0 = 0,\ y,\ z = w/2) = 2.4\,\mathrm{m/s}$. Immediately downstream the nozzle inlet, boundary layer development due to viscosity is seen to determine the shape of the transverse velocity profiles until the profiles become asymmetric at $x_0/h_0 = 1.8$ due to flow acceleration in the upstream vicinity of the obstacle. The asymmetry of the transverse profiles is characterised by a maximum velocity in the profile. The transverse position of the maximum velocity shifts from the vicinity of the wall $y = 0$, upstream from the obstacle, towards the opposite wall containing the obstacle as the flow reaches the obstacle.

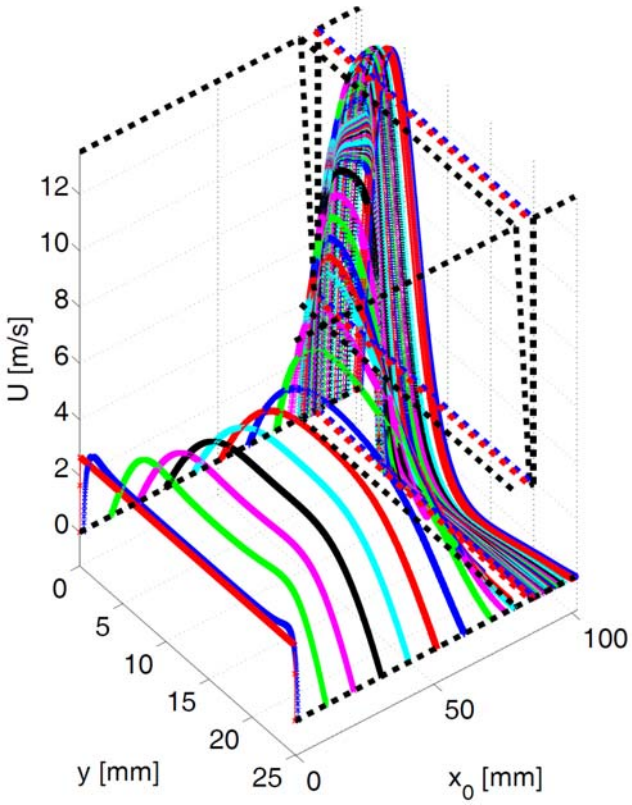

Figure 4. Transverse profiles of the simulated mean velocity in the plane $(x_0, y, z = w/2)$ are shown. For reasons of clarity, the geometry of the channel as function of x is schematically indicated (dotted lines). Recall that $y = 0$ corresponds to the flat channel wall.

Transverse profiles of the mean velocity are further detailed in Figure 5. Figure 5(a) shows transverse profiles of the mean velocity, $U(y/h_0)$, upstream, along and downstream from the obstacle. The asymmetry of the transverse profiles increases as x_0/h_0 approaches the obstacle. In addition, it is seen that the flow accelerates, so that a maximum velocity is reached downstream from the obstacle. Nevertheless, whereas upstream from the obstacle the position of maximum velocity shifts towards the bottom plate corresponding to $y/h_0 = 0$, the tendency is inversed within the constriction so

that the maximum velocity occurs close to the obstacles tip, i.e., $y/h_0 = 0.3$. Downstream from the obstacle, the position of the maximum velocity shifts away from the tip towards the flat wall and is situated in the neighborhood of $y/h_0 \approx 0.15$, which corresponds to the center of the constriction. Observed negative velocities for $y/h_0 > 0.3$ reveal the existence of a recirculation zone. The velocities in the recirculation zone are comprised between $-0.75\,\mathrm{m/s} < U < 0\,\mathrm{m/s}$. The profiles at the constriction and downstream the obstacle are further characterised in Figure 5(b) and Figure 5(c).

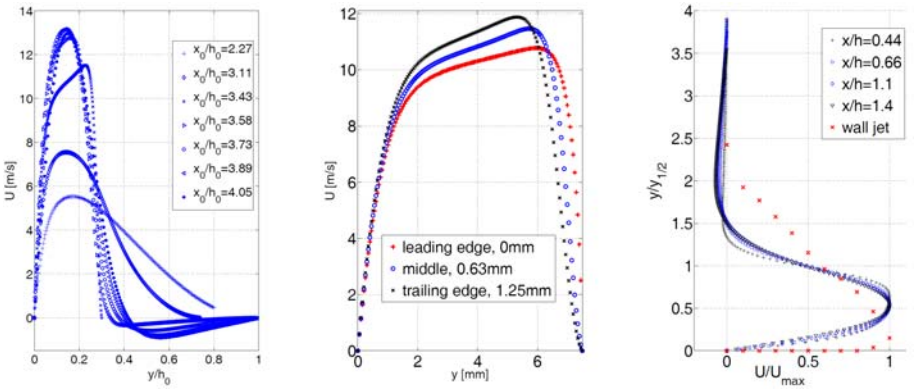

(a) $U(y/h_0)$ (b) $U(y)$ (c) $y/y_{1/2}(U/U_{\max})$

Figure 5. Overview of transverse profiles of the simulated mean velocity: (a) $U(y/h_0)$ upstream, at and downstream from the obstacle, (b) at the tip of the obstacle with length $l_t = 1.25\mathrm{mm}$, (c) mean transverse profiles in the near field downstream from the obstacle are represented in outer scaling, $y/y_{1/2}(U/U_{\max})$. As a reference typical experimental wall jet data, taken from [7], are indicated.

From Figure 5(b) it is seen that at the tips leading edge the maximum velocity is located immediately at the tip at $y/h = 1$ or $y = 7.5\mathrm{mm}$. As the flow continues to accelerates, the maximum velocity shifts slightly away from the tip and the asymmetry of the transverse profile increases.

Figure 5(c) shows transverse profiles of the mean velocity downstream from the obstacle. The velocity profiles are shown in outer scaling which is commonly used for wall jets [7, 18, 19, 10]: i.e., $y/y_{1/2}(U/U_{\max})$ with $U_{\max}$ denoting the maximum velocity in the transverse profile and $y_{1/2}$ the jet half width, defined as the transverse distance from the wall for which the velocity profiles yield $U(y_{1/2}) = U_{\max}/2$ with $y_{1/2} > y_m$ and y_m indicating the transverse position of the maximum velocity in the profile. It is observed that transverse jet profiles for $x/h > 0.44$ tend to collapse into a single curve. This finding suggests the development of a self-similar transverse profile of the mean velocity in the near field downstream from the obstacle despite the presence of the recirculation zone. Nevertheless, from Figure 5(c) it is seen that the shape of the self-similar profile in the near field downstream from the obstacle differs from a typical profile associated with a plane wall jet in the far field. Illustrated plane wall jet data are reported for $\mathrm{Re}_b = 9600$ and aperture of 9.6mm [7]. The ratio of the distance of the maximum velocity from the wall to the jet half width, $y_m/y_{1/2}$ yields $y_m/y_{1/2} = 0.57$ for the simulated data which is approximately twice the value reported for a typical wall jet, i.e., $0.15 < y_m/y_{1/2} < 0.17$ [7, 18, 33, 10, 5].

The simulated pressure distribution is illustrated in Figure 6(a). The total pressure drop ΔP equals the inlet pressure $P_0 = 72\mathrm{Pa}$ since the pressure at the outlet yields $P = 0\mathrm{Pa}$. Negative pressures are associated with the recirculation zone downstream from the obstacle. In addition, a small recirculation zone is observed immediately downstream from the obstacles leading edge where a pressure minimum of $-0.3 \times P_0$ occurs indicating flow separation and the presence of a small recirculation vortex. The simulated vorticity magnitude in the vicinity of the obstacle is illustrated in Figure 6(b). In general, the vorticity is seen to increase downstream from the obstacle along the wall and inside the outer shear layer due to the rapid changes of the velocity in these regions. In addition, the maximum vorticity is associated with the minimum pressure at the obstacles tip.

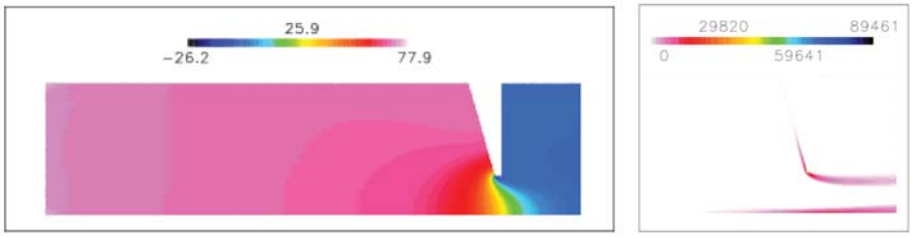

(a) Pressure distribution (b) Vorticity magnitude

Figure 6. (a) Simulated pressure distribution [Pa] and (b) simulated vorticity magnitude $[1/\mathrm{s}]$ in the neighborhood of the obstacle for the plane $(x_0,\ y,\ z = w/2)$.

Simulated streamwise x and transverse y root mean square velocities are shown in Figure 7. As for the mean velocity, the spanwise z component is negligible. The maximum of the root mean square velocity of 0.14m/s yields less than 10% of the maximum mean velocity of 13m/s as shown in Figure 3. In general, an increase of velocity fluctuations is associated with an increase and strong variation in mean velocity. Transverse profiles of the root mean square velocity normalised by the local mean streamwise velocity, representing the local streamwise turbulence intensity $T_{k=1}$ in the vicinity of the obstacle, are shown in Figure 8. The local turbulence intensity is less than 1% everywhere, except near the obstacle's tip where the local turbulence intensity exceeds 30% at a distance less than 0.1mm from the tip, i.e., $7.4 < y \leq 7.5\mathrm{mm}$. In general, from the root mean square velocity and local turbulence intensity it is seen that the turbulent regime is not reached. Nevertheless, the observed increased velocity fluctuations along the obstacles surface suggest that the interaction of the associated pressure fluctuations with the obstacle wall is a source of sound [4].

(a) x-component $\sigma_{k=1}$ (b) y-component $\sigma_{k=2}$

Figure 7. Simulated root mean square velocities σ_k [m/s] for the plane $(x_0,\ y,\ z = w/2)$: (a) x-component $\sigma_{k=1}$ and (b) y-component $\sigma_{k=2}$.

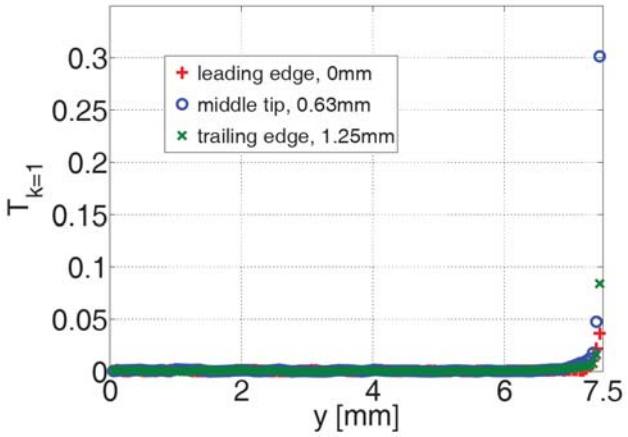

Figure 8. Transverse profile of local streamwise turbulence intensity $T_{k=1} = \sigma_{k=1}/U_{k=1}$ in the vicinity of the obstacle's tip for the plane $(x_0,\ y,\ z = w/2)$.

5.2. Flow in the vicinity and downstream from the obstacle: measured flow field

The flow downstream from the obstacle, from the trailing edge up to the nozzles exit $0 < x/h < 1.5$, is assessed numerically as well as experimentally. In addition, an overall view of the flow downstream from the nozzle exit $1.5 < x/h$ is obtained experimentally. Experimental flow characterisation from smoke experiments is derived based on the approach outlined in Section

4. A qualitative characterisation of the velocity field is obtained by processing the image flow field during smoke visualisation experiments whereas a quantitative characterisation of the velocity field is derived from PIV measurements. In the following, both approaches are represented using contours in order to facilitate comparison with respect to main features of the overall velocity field.

As indicated in Table 4, several visualisation windows are applied during smoke experiments in order to cover the region of interest. The velocity field in the vicinity of the obstacle $-2.1 < x/h < 3.2$ is studied in detail by PIV measurements illustrated in Figure 9. PIV measurements using the large camera window provide an overall view of the velocity field downstream from the nozzle $1.5 < x/h < 22$ as shown in Figure 10. Qualitative information is gathered from flow images in the region $0 < x/h < 7$ as depicted in Figure 11. All values derived from the PIV velocity fields and image flow fields are normalised with respect to their maximum value in order to facilitate comparison between qualitative and quantitative experimental flow characterisation.

The normalised magnitude of the mean velocity, root mean square velocity and vorticity in the vicinity of the obstacle $-2.1 < x/h < 3.2$ derived from PIV measurements is shown in Figure 9. PIV measurements confirm the general tendencies observed from numerical simulations: asymmetry of mean and root mean square velocity, flow separation at the leading edge of the obstacle and increased vorticity along the bottom plate and downstream from the obstacle's tip. Nevertheless, some differences between simulated and measured data in the vicinity of the obstacle's tip are revealed. A sharp peak in turbulence intensity up to 30% (Figure 8) and vorticity (Figure 6(b)) along the obstacle's tip are observed on the simulated data and not on the measured data because of the image resolution indicated in Table 4.

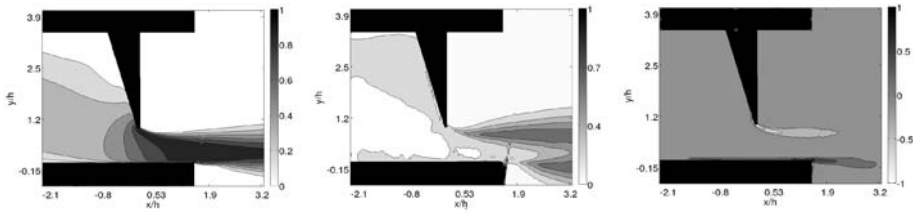

(a) $U^{piv}(x,\ y)$ (b) $U^{piv}_{rms}(x,\ y)$ (c) $\omega^{piv}(x,\ y)$

Figure 9. PIV measurements in the vicinity of the obstacle (full black): (a) normalised magnitude of the mean velocity $U^{piv}(x,\ y)$, (b) normalised root mean square of the velocity $U^{piv}_{rms}(x,\ y)$ and (c) normalised vorticity $\omega^{piv}(x,\ y)$.

In the near field downstream from the nozzle exit, illustrated in Figure 9, the flow separates from the bottom plate. Flow separation leads to a potential core region with parallel flow immediately downstream from the wall in which the jet does not spread. The core region is seen to be short $(\ll h)$ due to the ongoing development of the free outer shear layer downstream from the obstacle. As expected, jet spreading and root mean square velocity increase drastically near the end of the potential core due to development of the free shear layer. Moreover, from Figure 9(c) it is seen that flow separation at the bottom plate at the nozzle exit is associated with an increase in vorticity. The magnitude of the vorticity in this region is of the same order of magnitude as observed in the near field downstream from the obstacle's tip.

An overall view of the velocity field downstream from the nozzle exit in the region $1.5 < x/h < 22$ is obtained from PIV measurements. Figure 10 illustrates the normalised mean velocity, root mean square velocity and vorticity. In general, it is seen that the initial transverse asymmetry of the flow properties in the near field downstream from the nozzle exit reduces as the streamwise distance increases so that for $x/h > 10$ the flow field becomes quasi symmetrical. In the intermediate region $1.5 < x/h < 10$ asymmetric flow features occur due to the streamwise shift in flow separation

position which corresponds to the imposed distance between the obstacle tip and the nozzle exit defined by the parameter $l_0 = 11\text{mm}$ as indicated in Table 1. Asymmetrical jet spreading results in streamwise and transverse asymmetry of mean velocity, shear layer development and vorticity.

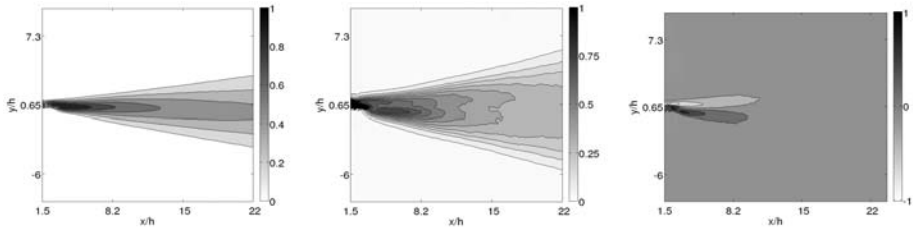

(a) $U^{piv}(x,\ y)$ (b) $U^{piv}_{rms}(x,\ y)$ (c) $\omega^{piv}(x,\ y)$

Figure 10. PIV measurements downstream the nozzle exit: (a) normalised magnitude of the mean velocity $U^{piv}(x,\ y)$, (b) normalised root mean square of the velocity $U^{piv}_{rms}(x,\ y)$ and (c) normalised vorticity $\omega^{piv}(x,\ y)$.

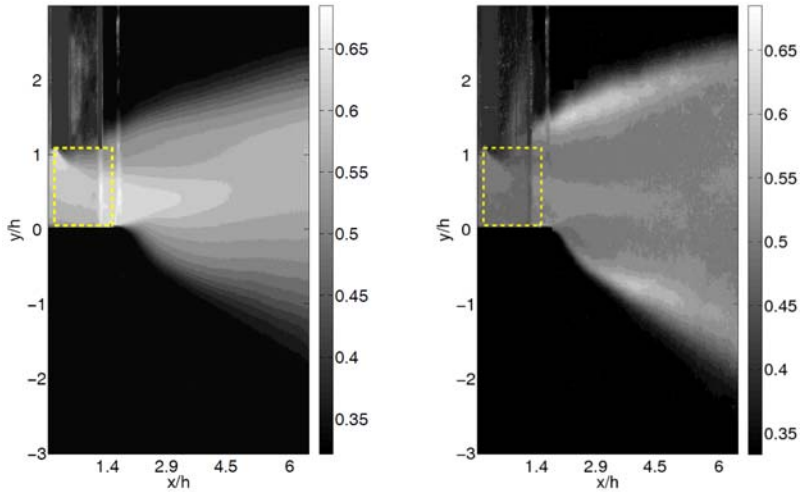

(a) $\bar{I}(x,\ y)$ (b) $I_{rms}(x,\ y)$

Figure 11. Image flow field in the range $0 < x/h < 7$ (a) mean smoke concentration $\bar{I}(x,\ y)$, (b) root mean square smoke concentration $I_{rms}(x,\ y)$. The dashed rectangle indicates the region $0 < x/h < 1.5$ between the obstacle's trailing edge and the nozzle exit.

Flow development downstream from the obstacle is qualitatively characterised by the mean and root mean square of the image flow fields illustrated in Figure 11 for the range $0 < x/h < 7$. As for the PIV measurements the observed order of events in streamwise direction is: flow separation at the obstacles tip, onset of outer shear layer development, flow separation at the nozzle exit and free shear layer development. Consequently, the flow field is asymmetrical and qualitative observations based on the image flow field matches the quantitative observations of the velocity field obtained from PIV measurements.

6. Discussion and Conclusion

An overall view of the velocity field through an asymmetrical teeth-shaped rectangular nozzle is presented for steady flow at $\mathrm{Re}_b = 4000$. The mean and fluctuating portion of the velocity field is qualitatively and quantitatively explored by visualizing numerical and experimental data obtained from large eddy simulation, smoke visualisation and PIV experiments. As such the current study, although exploratory, contributes to the study of moderate Reynolds number flows for which additional flow data are needed. Several conclusions can be made with respect to the flow development, with respect to the used methodology as well as with respect to applications such as human sibilant fricative production:

The presence of the trapezoid obstacle causes flow acceleration and flow separation, firstly within the nozzle at the leading edge of the obstacle's tip and secondly at the nozzle's exit at the bottom plate, so that the flow development is highly asymmetrical:

- Due to flow separation at the obstacle's tip a free outer shear layer develops whereas the flow is still bounded by the bottom plate resulting in an inner boundary layer so that the flow structure is three layered consisting of an inner boundary layer, core region and outer boundary layer. Based on transverse profiles the flow in this region, i.e., immediately downstream from the obstacle's trailing edge up to

the nozzles exit, is suggested to be self-similar although the classic wall jet profile is shown not to hold.

- The jet formed by flow separation downstream from the flat bottom plate is characterised by a short potential core region, i.e., $\ll h$, followed by the onset of a turbulent jet and free shear layer development. The short potential core extent is due to the presence of the outer shear layer, which induces turbulence production and convection and favours the interaction of the shear layers. Consequently, compared to plane jets, the onset of turbulent jet formation is shifted upstream towards the nozzle exit. Moreover, the observed asymmetry in the mean velocity profile in the core region of the wall bounded jet immediately downstream from the obstacle is likely to favor jet instability. Consequently, the presence of the obstacle results in a complex flow development which remains highly asymmetrical up to 10 times the aperture h downstream from the obstacle, i.e., $10 \times h$.

- Regions of increased vorticity are experimentally observed to be associated with flow separation. Consequently, the asymmetry in the velocity field and the streamwise assymetry in flow separation positions - at the obstacle tip and at the nozzle exit - result in an asymmetrical vorticity field as well.

The current study points out the severe impact of the obstacle on the flow field. Nevertheless, the study is exploratory since several questions can be raised with respect to the influence of the geometrical nozzle parameters on the flow development and more in particular on the development of the shear layers and their interaction. Obviously, additional geometrical configurations need to be studied in order to fully understand and demonstrate the influence of constriction degree, obstacle shape (angles, thickness) and distance between the obstacle's trailing edge and the nozzle exit. The last parameter is of particular interest since it dictates the streamwise asymmetry in flow separation position and therefore in shear layer development.

The simulated local turbulence intensity is less than 1% for almost the entire flow domain, so that it is concluded that the turbulent regime is not reached within the nozzle. Nevertheless, increased rms velocities are observed at the leading tip of the obstacle and the local simulated turbulence intensity increases up to 30%. The simulated vorticity increases at the obstacles tip as well. The increase of vorticity is confirmed experimentally from PIV measurements. The turbulence intensity increase up to 30% at the obstacle tip is not confirmed experimentally. Experimental data reveal in addition a strong increase in vorticity downstream from the nozzle. Regions of increased vorticity are likely to be associated with sound sources. Consequently, the relationship between sound sources and measurable geometrical parameters need to be studied in more detail.

Although a severe simplification of upper incisors in the human oral tract, the current exploratory study illustrates the benefit of simplified geometries for the study of applications such as human sibilant fricative sound production. In particular, the use of simplified geometries for which both numerical and experimental data are assessed, allows to study the relationship between geometrical parameters, flow properties and eventually sound properties in a systematic and reliable way.

Appendix

A. Flow modeling

The airflow is simulated with Large Eddy Simulation (LES) for incompressible unsteady flows [20, 31]. The spatially-filtered momentum equation (1) and continuity equation (2) are solved over the discretised flow domain described in Section 3,

$$\frac{\partial \overline{u}_i}{\partial t} + \frac{\partial}{\partial x_j}(\overline{u}_i \overline{u}_j) = -\frac{1}{\rho_0}\frac{\partial \overline{p}}{\partial x_i} + \nu \frac{\partial}{\partial x_j}\left(\frac{\partial \overline{u}_i}{\partial x_j} + \frac{\partial \overline{u}_j}{\partial x_i}\right) - \frac{\partial \tau_{ij}}{\partial x_j}, \qquad (1)$$

$$\frac{\partial \overline{u}_i}{\partial x_j} = 0, \qquad (2)$$

where $\overline{u}_i$ are the grid-scale velocity components $(i = 1, 2, 3)$, $\overline{p}$ is the grid-

scale static pressure and τ_{ij} is the subgrid scale (SGS) stress tensor. The physical parameters of the model are set to density $\rho_0 = 1.2\text{kg.m}^{-3}$ and kinematic viscosity $\nu = 1.5 \times 10^{-5}\text{m}^2.\text{s}^{-1}$ as indicated in Table 3. A second-order Crank-Nicolson scheme (implicit method) is used for the discretisation of the momentum equation. The unknowns $\overline{u}_i$ and $\overline{p}$ result from the decomposition of the velocity and the pressure into a resolvable ($\overline{u}_i$ and $\overline{p}$) and subgrid scale part (u_i' and p') as:

$$u_i = \overline{u}_i + u' \text{ and } p = \overline{p} + p'.$$

The SGS stress tensor τ_{ij} groups all terms which are not exclusively dependent on the large scale, so that:

$$\tau_{ij} = \overline{u}_i\overline{u}_j - \overline{u_i u_j}.$$

The subgrid scale turbulence is modelled with the Smagorinsky closure model, which is based on the formulation of the subgrid scale stress as:

$$\tau_{ij} - \frac{1}{3}\tau_{kk}\delta_{ij} = -2\nu_{SGS}\overline{S}_{ij},$$

with $\overline{S}_{ij}$ denoting the strain rate tensor and ν_{SGS} the subgrid scale eddy viscosity, which are defined by:

$$\overline{S}_{ij} = \frac{1}{2}\left(\frac{\partial\overline{u}_i}{\partial x_j} + \frac{\partial\overline{u}_j}{\partial x_j}\right) \text{ and } \nu_{SGS} = (C_S\Delta)^2\sqrt{2\overline{S}_{ij}\overline{S}_{ij}},$$

with Smagorinsky constant C_S. The size of the grid filter Δ is defined locally from the discretised volume as:

$$\Delta = \sqrt[3]{\text{Element Volume}}.$$

The Smagorinsky constant C_S is calculated locally in space and time using Lilly's least square procedure [11, 21]. The pressure field is computed from the velocity field using the fractional step method.

The spatial distribution of turbulence is computed from the instantaneous velocity fields U^i and the mean velocity U as the root mean square (rms) velocity denoted σ_k,

$$\sigma_k = \sqrt{\frac{1}{N_m}\sum_{i=1}^{N_m}(U_k^i - U_k)^2}, \tag{3}$$

with $k = 1$ the longitudinal x-component, $k = 2$ the transverse y-component, $k = 3$ the spanwise z-component and $N_m = 5200$ the number of time steps taken into account. The local turbulence intensity T_k is defined as the ratio of the root mean square velocity σ_k to the mean velocity U_k at a given position,

$$T_k = \frac{\sigma_k}{U_k}. \tag{4}$$

The vorticity is derived as the curl of the velocity field, $\omega = \nabla \times \overline{U}$.

B. Quantitative and qualitative smoke experiments

In order to perform flow visualisation buoyant white smoke is injected in the settling chamber shown in Figure 2 by means of a fog machine. Next, quantitative and qualitative smoke experiments are obtained by considering the image and velocity flow field as outlined in the following sections.

B.1. Qualitative smoke experiment: image flow field

A two-dimensional laser light beam is generated by a laser light source (class IIIb). To record the illuminated smoke pattern, a color camera is positioned perpendicular to the laser sheet. Instantaneous images are recorded at 300fps. The digitised images are 1280×720 data matrices. Spatial calibration of the images is performed.

Individual images are processed in order to estimate the instantaneous spatial distribution of smoke concentration. The image data matrices are reduced to the region of interest and a background image is subtracted. Next, each image color data matrix (x, y) is conversed to a gray-level data matrix

$I_{gray}(x, y)$. The gray scale histogram $I_{gray}(x, y)$ of each image is then stretched to occupy the full range from 0 to 255 as:

$$I(x, y) = \frac{I_{gray}(x, y) - I_{\min}}{I_{\max} - I_{\min}} \times 255, \tag{5}$$

in which *I* indicates the intensity and the subscripts *min* and *max* denote the minimum and maximum values of the image's histogram.

The mean and fluctuating histogram statistics are determined from the stretched gray scale images as:

$$\bar{I}(x, y) = \frac{1}{n}\sum_{i=1}^{n} I_i(x, y), \tag{6}$$

$$I_{rms}(x, y) = \sqrt{\frac{1}{n}\sum_{i=1}^{n}(I_i(x, y) - \bar{I}(x, y))^2}, \tag{7}$$

in which $n = 4500$ denotes the number of instantaneous flow images taken into account and the sub-script *rms* indicates root mean square value.

B.2. Quantitative smoke experiment: velocity flow field

The velocity field is quantified using Particle Image Velocimetry (PIV) [2]. Smoke particles with a mean diameter of 2μm are obtained from a smoke generator (Antari) and a solution of water and glycerine. A dual Nd-YAG laser (class IV) is used to create the laser sheet and to illuminate the smoke particles. Spatially calibrated images of the particles are taken by a CCD camera with 1376×1024 pixels. Postprocessing of the images is done using a commercial software (Lavision Davis 7). Interrogation windows are 16×16 pixels. A multipass algorithm is used, starting from a 64×64 pixels window, with a 50% overlap. Hence the spatial resolution of the measurement in the streamwise direction Δx_{PIV} is estimated by dividing the length of the measurement zone in the streamwise direction by the total number of pixels, 1376, and then remultiplying by 8 pixels, which is 50% of

16 pixels. Consequently, in case the length of the measurement zone yields approximatively 5cm the spatial resolution yields $\Delta x_{PIV} \approx 0.3$mm. In the same way, the transverse spatial resolution yields $\Delta y_{PIV} \approx 0.3$mm in case the transverse height of the measurement zone is set to approximately 4cm.

The time separation *Dt* between two laser pulses is chosen to meet the criterion on maximal particle displacement within the interrogation window [2]. This criterion states that the displacement of the seeding particles between two images should not exceed one quarter of the interrogation window, which is $16/4 = 4$ pixels. For the current Reynolds number $\mathrm{Re}_b = 4000$, the time separation between two laser pulses is set to $Dt = 50\mu$s. The flow is quantified on 2000 pair of images, which provides 2000 instantaneous velocity vector fields $U_i(x, y)$. In the same way as for the image flow field $I_i(x, y)$ in equation (6) and equation (7), mean and fluctuating velocity vector statistics are obtained by averaging the 2000 instantaneous vector fields and by calculating the root mean square value. The same way as for the simulated flow field other quantities such as the vorticity are derived from the measured two-dimensional velocity fields. The experimentally quantified mean velocity, root mean square of the velocity and vorticity are denoted U^{piv}, U_{rms}^{piv} and ω^{piv}, respectively.

References

[1] S. Adachi and K. Honda, CFD approach to fricative sound sources, Proc. 6th International Seminar on Speech Production, pp. 1-4, Sydney, Australia, 2003.

[2] R. J. Adrian, Dynamic ranges of velocity and spatial resolution of particle image velocimetry, Meas. Sci. Technol. 8 (1997), 1397-1398.

[3] D. J. Bodony, The prediction and understanding of jet noise, Center for Turbulence Research Annual Research Briefs, 2005, pp. 367-377.

[4] S. Curle, The influence of solid boundaries upon aerodynamic sound, Phil. Trans. R. Soc. Lond. A 231 (1955), 505-514.

[5] A. Dejoan and M. Leschziner, Large eddy simulation of a plane turbulent wall jet, Phys. Fluids 17 (2005), 1-16.

[6] E. Ellis and J. A. McNamara, Cephalometric evaluation of incisor position, Angle Orthodontist 56 (1989), 324-344.

[7] J. Eriksson, R. Karlsson and J. Person, An experimental study of a two-dimensional plane turbulent wall jet, Exp. Fluids 20 (1998), 50-60.

[8] G. Fant, The Acoustic Theory of Speech Production, Mouton, The Hague, 1960.

[9] C. D. Fredericks, A method for determining the maxillary incisor inclination, Angle Orthodontist 44 (1974), 341-345.

[10] W. George, H. Abrahamsson, J. Eriksson, R. Karlsson, L. Lofdahl and M. Wosnik, A similarity theory for the turbulent plane wall jet without external stream, J. Fluid Mech. 425 (2000), 367-411.

[11] M. Germano, U. Piomelli, P. Moin and W. Cabot, A dynamic subgrid-scale eddy viscosity model, Phys. Fluids A 3 (1991), 1760-1765.

[12] X. Grandchamp, Modélisation physique des écoulements turbulents appliquées aux voies aériennes supérieures chez l'humain, Ph.D. Thesis, Grenoble University, 2009.

[13] Y. Guo, C. Kato and Y. Yamade, Basic features of the fluid dynamics simulation software FrontFlow/Blue, Japanese Society Fluids Mechanics 58 (2006), 11-15.

[14] R. Haralick and L. Shapiro, Computer and Robot Vision, Addison-Wesley Publishing Company, 1992.

[15] M. Howe and R. McGowan, Aeroacoustics of [s], Proceedings Royal Society A 461 (2005), 1005-1028.

[16] C. Kato and M. Ikegawa, Large eddy simulation of unsteady turbulent wake of a circular cylinder using the finite element method, ASME-FED 117 (1991), 49-56.

[17] M. Krane, Aeroacoustic production of low-frequency unvoiced speech sounds, J. Acoust. Soc. Am. 118(1) (2005), 410-427.

[18] B. Launder and W. Rodi, The turbulent wall jet, Prog. Aerospace Sci. 19 (1955), 81-128.

[19] B. Launder and W. Rodi, The turbulent wall jet: measurement and modeling, Ann. Rev. Fluid Mech. 15 (1983), 429-459.

[20] M. Lesieur, O. Métais and P. Comte, Large-eddy Simulations of Turbulence, Cambridge University Press, New York, 2005.

[21] D. Lilly, A proposed modification of the Germano subgrid-scale closure method, Phys. Fluids 4 (1992), 633-635.

[22] T. Liu and L. Shen, Fluid flow and optical flow, J. Fluids Mechanics 614 (2008), 253-291.

[23] P. Magne, G. O. Gaulluci and U. C. Belser, Anatomic crown width/length ratios of unworn and worn maxillary teeth in white subjects, J. Prosthetic Dentistry 89 (2003), 453-461.

[24] G. R. McIntyre and D. T. Millett, Lip shape and position in class II division 2 malocclusion, Angle Orthodontist 76 (2006), 739-744.

[25] W. Merzkirch, Flow Visualization, Academic Press, London, UK, 1987.

[26] J. Mi, R. Deo and G. Nathan, Characterization of turbulent jets from high-aspect-ratio rectangular nozzles, Phys. Fluids 17 (2005), 4.

[27] K. Nozaki, T. Akiyama, H. Tamagawa, S. Kato, Y. Mizuno-Matsumoto, M. Nakagawa, Y. Maeda and S. Shimojo, The first grid for the oral and maxillofacial region and its application for speech analysis, Meth. Inf. Med., 2005, pp. 253-256.

[28] G. Ramsay, The influence of constriction geometry on sound generation in fricative consonants, Proc. Acoustics08, Paris, France, 2008, pp. 1-4.

[29] D. J. Rudolph, P. D. Dominguez, K. Ahn and T. Thinh, The use of tooth thickness in predicting intermaxillary tooth-size discrepancies, Angle Orthodontist 68 (1998), 133-140.

[30] C. Runte, M. Lawerino, D. Dirksen, F. Bollman, A. Lamprecht-Dinnsen and E. Seifert, The influence of maxillary central incisor position in complete dentures on /s/ sound production, J. Prosthetic Dentistry 85 (2001), 485-495.

[31] P. Sagaut and M. Germano, Large Eddy Simulation for Incompressible Flows, Spring Verlag, New York, 2005.

[32] H. Schlichting and K. Gersten, Boundary Layer Theory, Springer Verlag, Berlin, 2000.

[33] M. E. Schneider and R. J. Goldstein, Laser Doppler measurement of turbulence parameters in a two-dimensional plane wall jet, Phys. Fluids 6 (1997), 3116-3129.

[34] C. Shadle, The acoustics of fricative consonants, Ph.D. Thesis, 1985.

[35] C. Shadle, M. Berezina, M. Proctor and K. Iskarous, Mechanical models of fricatives based on MRI-derived vocal tract shapes, Proc. 8th International Seminar on Speech Production, Strasbourg, France, 2008, pp. 417-420.

[36] D. Sinder, Speech synthesis using an aeroacoustic fricative model, Ph.D. Thesis, 1999.

[37] K. M. Smith and J. C. Dutton, A procedure for turbulent structure convection velocity measurements using time-correlated images, Exp. Fluids 27 (1999), 244-250.

[38] K. Stevens, Acoustic Phonetics, MIT Press, London, 1998.

[39] P. T. Tokumaru and P. E. Dimotakis, Image correlation velocimetry, Exp. Fluids 19 (1992), 1-15.

[40] A. Van Hirtum, X. Pelorson, O. Estienne and H. Bailliet, Experimental validation of flow models for a rigid vocal tract replica, J. Acoust. Soc. Am. 130 (2011), 2128-2138.